Joining of nickel-base superalloy single crystals

S. S. Babu, S. A. David, J. W. Park, and J. M. Vitek

Metals and Ceramics Division, Oak Ridge, TN 37831-6096, USA

Internet: http://mjndeweb.ms.ornl.gov

Introduction

Welding is necessary for rejuvenation and repair of single-crystal nickel-base superalloy components of gas turbines.[1] Welding is essential for (1) removal of defects that have been introduced during casting and subsequent processing and (2) repair of the components that are worn or damaged during service. In general, the repairs are made by fusion-welding techniques, including gas-tungsten-arc, microplasma, electron-beam, and laser-beam welding techniques.[2] The welds are either autogenous or made with the addition of filler metal, depending upon the joint geometry. In addition, the buildup of parts can be accomplished by diffusion joining techniques, such as transient-liquid-phase bonding.[3,4] Feasibility of both rejuvenation and repair processes is decided by the ability to produce desired microstructures that yield required service properties. A flow chart of rejuvenation and repair processes is shown in Fig. 1. Not every step shown in the Fig. 1 is well standardized; therefore, there is a need to evaluate the change in microstructure and properties of nickel-base superalloy components at every step by experimental characterization and theoretical models. In the last decade, Oak Ridge National Laboratory (ORNL) has been involved in a systematic investigation of both technical and scientific issues related to fusion welding of single-crystal iron- and nickel-base superalloys. In this paper, an overview of past and current research on the weldability of single-crystal nickel-base superalloys at ORNL is presented. The reader is referred to various publications by the authors for details.[2,5,6,7,8,9]

Overview of Weldability of Nickel-Base Superalloys

The weldability and microstructure evolution in single-crystal PWA-1480 alloy [Ni - 5.0 Al - 10.0 Cr - 1.5 Ti - 5.0 Co - 12.0 Ta - 4.0 W (wt %)] and CMSX4 alloy [Ni - 5.5 Al - 6.5 Cr - 1.0 Ti - 7.0 Co - 7.0 Ta - 6.5 W (wt %)] have been investigated before.[2] During electron-beam welding of PWA-1480 single crystals, extensive centerline cracking was observed in the weld metal region, as shown in Fig. 2. Detailed microstructure analysis indicated epitaxial growth of the base metal took place. However, near the center of the weld metal region, the single-crystalline nature was compromised by the formation of stray grains, as indicated by arrows in

Fig. 2. In addition, centerline cracks were associated with the stray grains. Preheating the base metal to 500°C before welding reduced this cracking tendency. Careful analysis showed that the preheating did not remove the stray grains,. Therefore, mitigation of cracking with preheating is related to reduction of thermal stresses. Related research on welding of single-crystal CMSX-4 alloy showed that successful welds could be obtained by pulsed-laser welding without preheats. Most of the cracking was associated with the formation of stray grains. Extensive research on PWA-1480 welding optimization by changing the speed, direction, and preheat led to the following conclusions.[2,8] (1) Welding direction had no effect on the weld cracking. However, there were changes in the solidification dendrite patterns. (2) Welding speed affected the weld pool shape and size. (3) Preheating to 500°C and slow welding speeds reduced the cracking tendency. However, preheating and high welding speeds still led to weld cracking. (4) In the case of laser welding, the pulse rate did not change the cracking tendency. High laser pulse rates, for a given welding speed, led to the formation of a continuous weld. In contrast, small pulse rates led to the formation of overlapping spot welds. Crack-free laser welds were obtained only at slow welding speeds.

During these investigations, there was a need to understand the mode of weld cracking in these alloys. However, identification of cracking during welding is difficult because of the presence of a bright arc. This difficulty was overcome by using a specialized in situ weld-monitoring system.[7] This system allowed us to illuminate the weld area with stroboscopic light and thus to monitor the weld area even in the presence of a bright arc. The welds were made on an experimental single-crystal alloy by a gas-tungsten-arc welding process in a SigmaJig[10] weld restraint system that applied a stress of 68 MPa. The setup and the results obtained from an experimental single-crystal superalloy are shown in Fig. 3. The figure shows a series of four images recorded by the camera at different time intervals: (1) the passage of the arc (0.09 s), (2) the solidified weld pool (1.19 s), (3) the onset of transverse weld cracking (2.30 s), and (4) the completely cracked weld (3.06 s). An important observation is that the initiation of a crack was observed nearly 1.11 s after the completion of weld solidification. An additional observation is that the cracks were in the transverse direction to that of the welding direction. The transverse cracking is in contrast to the observed longitudinal centerline cracking in other single-crystal

alloys during weld-pool solidification. The complex cracking tendencies observed in these alloys were related to the interactions between metallurgical susceptibility and transient stress conditions during weld heating and cooling.[9] The above research demonstrated that the weldability of single-crystal nickel-base superalloys is related to complex interactions among crystallography, solidification grain structure, and solid-state transformations. The following sections discuss each one of these with examples.

Crystallography

The orientation of actively growing <001> dendrites in nickel-base superalloys is influenced by their orientation with respect to the liquid-solid boundary. Rappaz et al. have developed a geometrical model to describe the selection of growth variants as a function of three-dimensional weld pool shapes.[11,12] To determine the specific variant of <100> for a given location, the velocities of these dendrites ($\vec{V}_{hkl}$) are calculated with the following relation:

$$\left|\vec{V}_{hkl}\right| = \left|\vec{V}_{weld}\right|\frac{\cos\theta}{\cos\psi} \ . \tag{1}$$

In Eq. (1), θ is the angle between the normal to the liquid-solid interface $\vec{n}$ [shown in Fig. 4(a)], and the vector representing the welding direction ($\vec{V}_{weld}$), and ψ is the angle between $\vec{n}$ and dendrite growth direction ($\vec{V}_{hkl}$). In this paper, this model has been extended to any arbitrary weld pool shape through numerical methods. It can also be used to analyze the selection of dendrite growth variants as well as the velocity of these dendrites perpendicular to the liquid-solid interface front.[13] A typical calculation using the above model for the dendrite growth selection in a PWA-1480 alloy is presented here. A transverse cross section of a PWA-1480 electron-beam weld similar to that shown in Fig. 2 is analyzed [see Fig. 4(b)]. In this weld, the welding direction is [100] and the surface normal direction is [001]. The dendrite orientations in this weld are interpreted based on the morphology. The analyses showed that the regions of [0$\bar{1}$0], [010], and [001] dendrite orientations can be clearly identified [see Fig. 4(c)]. However, the analysis also showed stray grains in the regions (marked as "s") where the predominant growth direction was expected to be of [001] type. To evaluate this dendrite growth mode, a three-dimensional weld pool shape was described as shown in Fig. 4(d). The cross section of the

weld was used to get the z and y coordinates of weld pool. A semicircular weld pool shape at any given depth was assumed because the welding was done in the keyhole mode. Therefore, the ratio of maximum weld pool width (y_{max}) to maximum weld length (x_{max}) is one for all values of z. If this weld pool shape is used, the θ and ψ (ψ is related to θ and ϕ the angle between the y-axis and the projection of $\vec{n}$ on the y-z plane) can be calculated for all positions on the weld pool solidification front. The dendrite growth directions and their respective velocity ratio, $\left|\vec{V}_{hkl}\right|/\left|\vec{V}_{weld}\right|$, based on the geometrical model are shown in Fig. 4(e) for all possible values of θ and ϕ. The information is now applied to the entire liquid-solid interface as the weld pool solidification occurs [see Fig. 4(f)]. The predictions of the geometrical model agree qualitatively with observations for the epitaxial growth of dendrites in $[0\bar{1}0]$ and $[010]$ directions from the base metal. The extent of this growth into the weld was under-predicted (i.e., predictions showed less extension of $[0\bar{1}0]$ and $[010]$ toward the center of the weld than observed). The predicted [001]-dendrite growth zones are in agreement with the interpretations in Fig. 4(c). Interestingly, the experimentally observed [001] dendrites appear to extend into the [100] growth regions, and the stray grains appear to be present always in the predicted region for the [100] growth. The velocities in the [001] zones are indeed the highest (velocity ratio equal to one), i.e., velocity of dendrites is equal to welding velocity. The tendency for stray grain formation can be related to dendrite growth velocity, temperature gradient, and the amount of undercooling below the equilibrium liquidus temperature; this will be discussed in the next section. Theoretical treatment indicates that, for a given temperature gradient, there will be a higher probability of equiaxed dendrite growth ahead of the dendritic liquid-solid interface with an increase in interface velocity. Therefore, the present geometrical model allows one to predict the tendency for stray grain formation to a certain extent.

The above model can be extended to investigate the cracking tendency in autogenous laser welds of single-crystal nickel-base superalloy N5 (Ni-7.5Co-7Cr-1.5Mo-5W-3.00Re-6.5Ta-0.15Hf) with two different welding speeds (4.2 and 12.7 mm/s). Surface views of the weld and the base metal are shown in Figs. 5(a) and (b). In this case, the welding direction was [0.141, $\overline{0.217}$, 0.966] and surface normal was [$\overline{0.925}, \overline{0.376}$, 0.051]. The welds made at a speed of 4.2 mm/s

showed no cracking tendency even though they showed stray grains. In contrast, the welds made at a speed of 12.7 mm/s showed extensive cracking and stray grains. Interestingly, the cracks were observed on only one side of the weld.[14] The dendrite growth directions were predicted by using the geometry model. The results for both welds are shown in Fig. 5(*c*) and (*d*). During the analysis, the experimentally observed transverse cross sections of welds were used to obtain the *y* and *z* coordinates of the weld pool shape. The length of the weld pool was calculated from heat transfer models.[14] Welding directions in these images are from bottom to top. The model predicted growth of $[0\bar{1}0]$ dendrites from the left side of the weld toward the center of the weld for a large distance but limited growth of [010] dendrites from the right side of the weld into the centerline at a 4.2 mm/s welding speed. This indicates that the dendrite growth on the right side of the weld must be predominantly governed by [001] oriented dendrites. The predictions for the high-speed weld showed that the growth of [010] dendrites will be even less favored and that the predominantly [001] dendrites will be favored on the right side of the weld. However, the experimental microstructure shows extensive stray grain formation. In addition, high-magnification micrographs of the surface [Fig. 5(*e*)] and a transverse section [Fig. 5(*f*)] show that the extent of the $[0\bar{1}0]$ dendrite is larger than the value predicted by the geometrical model. This is attributed to the simplifications in assumed shape of the weld pool. Therefore, the above results suggest that the geometrical model can predict the trends but not the true extent of dendrite growth, probably due to temporal variations and inaccuracies of the weld pool shape. Further work is under way to investigate the effect of weld pool shape on dendrite growth orientations. The mechanism for cracking in the presence of stray grains must also be related to the generation of tensile thermal stresses, which will be discussed in the later section.

Solidification Grain Structure

Microstructural observations indicate that cracks are often associated with stray-crystal formation. Therefore, it is highly desirable to reduce the occurrence of these stray crystals. Because there are only a few of these grains, the total high-angle grain boundary area is small. In the presence of a low-melting eutectic liquid during solidification and such a small high-angle grain boundary area, the extent of grain boundary wetting will be large. Therefore, the tendency to form cracks in the presence of stress is enhanced. The formation of stray grain formation and

its relation to cracking was further studied in previous research.[7] During welding of Fe-Cr-Ni single crystals, stray crystals were not observed. However, upon doping Fe-Cr-Ni welds with sulfur, stray crystals formed in these welds. The mechanism for the formation of stray crystals in welds was related to solidification conditions. The stray-crystal formation can be interpreted based on the degree of constitutional supercooling that is present ahead of the dendrite tip. The original model by Hunt[15] was recently extended by Gaumann et al., who used solidification theories to describe undercooling as a function of distance from the tip of the dendrite.[16] In this model, the concentration profile predicted by the Ivantsov function[17] is used to describe the local liquidus temperature, $T_{comp}^{liquid}\{z\}$, as a function of distance, z, from the dendrite tip. The final form of this variation is given as follows:

$$T_{comp}^{liquid}\{z\} = T_0^{liquid} + (T_{Tip}^{liquid} - T_0^{liquid})E\{P_c, z, R\} \ , \qquad (2)$$

where T_0^{liquid} is the liquidus temperature alloy for the nominal composition far away from the dendrite tip, P_c is the solutal Peclet number, R is the dendrite tip radius, T_{Tip}^{liquid} is the dendrite tip temperature calculated by using the interface response function models, and $E\{P_c, z, R\}$ is the integral exponent function. The local liquid temperature for a given temperature gradient (G_L) as a function of distance (z) from the dendrite tip is given by

$$T_{local}^{liquid} = T_{Tip}^{liquid} + G_L z \ . \qquad (3)$$

With Eqs. (2) and (3), it is now possible to determine the constitutional supercooling which relates to the tendency for strain grain formation as a function of distance which is given by

$$\Delta T_{constitutional} = T_{comp}^{liquid} - T_{local}^{liquid} \ . \qquad (4)$$

The reader is referred to the reference 16 for more details on the prediction. A schematic illustration of the region ahead of the dendrite tip that is capable of forming equiaxed stray grains is shown in Fig. 6. Within the shaded region in the top graph, the local temperature is lower than the liquidus temperature of the alloy and may lead to homogeneous nucleation of equiaxed dendrites. This region will be reduced even more by the extent of additional undercooling needed to nucleate the grains. Current research is underway to extend this criterion to a three-

dimensional weld pool shape by coupling it with a crystallographic geometry model[13] and a numerical heat transfer model[14] to describe tendency for stray grain formation throughout the weld pool. However, these extensions must consider the constraints of solidification theory for multicomponent alloy including the necessity to have tie lines passing through the bulk composition, equal diffusion coefficient and back diffusion in the solid.

Recently, the grain structures in gas-tungsten-arc spot-welds of similar dimensions but with two different cooling rates were studied to elucidate the interactions of crystallography and the velocity of the liquid-solid boundary. The spot welds were made by a stationary arc with a hold time of 15 s on a TMS75 [Ni-6Al-12Co-3Cr-2Mo-5Re-6Ta-6W-0.1Hf (wt %)] single-crystal nickel-base superalloy. After the hold time, one of the welds [see Fig. 7(*a*)] was cooled rapidly by sudden extinction of the welding arc. In the other weld, the arc current was reduced gradually over 25 s, leading to slow cooling of the weld [see Fig. 7(*b*)]. The rapidly cooled weld was expected to produce a high interface velocity in comparison to the slowly cooled weld. The micrograph shows large variations in dendrite growth orientations and some tendency for stray grain formations; the cracks were always associated with a change in dendrite growth orientations. The above phenomenon is being studied further with theoretical modeling involving a crystallographic geometric model and constitutional supercooling models described earlier.

Solid-State Transformations

Previous transmission electron microscopy (TEM) investigations of PWA-1480 welds showed well-developed cuboidal γ′ precipitate morphology [see Fig. 8(*a*)] within the γ grains as well as eutectic γ+γ′ microstructure along the dendrite boundaries in the as-welded condition.[5] This microstructure was similar to that observed in the base metal. In addition, atom probe field ion microscopy (APFIM) revealed that the compositions of γ and γ′ phases in PWA-1480 electron-beam welds were similar to those in the base metal. In contrast, the CMSX-4 welds made by pulsed-laser welding without preheat showed an irregular γ′ precipitate morphology and a negligible amount of eutectic γ+γ′ microstructure along the dendrite boundary [see Fig. 8(*b*)]. The weld microstructure was quite different from that of the base metal microstructure.[6] The APFIM analyses showed large concentration gradients in the γ phase near the γ-γ′ interface. The

above microstructural differences were attributed to the rapid weld-cooling conditions during pulsed-laser welding.

The decomposition of γ phase into γ+γ´ phase mixture is more or less similar in directionally solidified and single-crystal alloys. Therefore, recent research focused on the decomposition of γ phase into γ+γ´ phase in a directionally solidified CM247 alloy [Ni - 8.0 Cr - 9.0 Co - 5.5 Al - 0.8 Ti - 0.1 Nb - 0.6 Mo - 3.2 Ta - 9.5 W - 0.08 C (wt %)]. The decomposition of of γ phase into γ+γ´ phase mixture was investigated in this alloy under a different cooling rate from solutionizing temperature of 1300°C.[18] The results showed that with an increase in cooling rate, the number density of primary γ´ precipitates increased, the size of γ´ precipitates decreased, and the shape of γ´ precipitates progressively changed from cuboidal to an irregular and or spherical nature. The base metal samples after standard heat treatment have regular cuboidal precipitates as shown in Fig. 9(*a*). The precipitates in the water-quenched condition [Fig. 9(*b*)] were very different and irregular. The reasons for the drastic change in precipitate morphology in the water-quenched condition were analyzed further with atom probe tomography. A chromium atom map obtained from atom-probe tomography analysis of a water-quenched sample is shown in Fig. 9(*c*). The Cr-enriched γ phase (dark) and the Cr-depleted γ´ phase regions (light) can be easily identified. The atom maps indicated that the γ´ morphology does not conform to a cuboidal or spherical γ´ precipitate. The image shows a very thin γ region (marked "A") and a comparatively thicker γ region (marked "B"). The chromium concentration gradients in these regions were further analyzed and the iso-concentration surfaces at 15 at. % Cr are shown in Figs. 9 (*d*) and (*e*). The surfaces in the region A have holes [see Fig 9(*a*)] indicating the γ´ precipitates on either side are connected to each other. The average Cr concentration in a small-volume element within this thin γ region was less than ~12 at. % This discontinuity suggests that the γ´ precipitates on either side of this γ phase region are interconnected. The observation agrees with the complex interconnected morphology of γ´ precipitate observed in TEM micrographs. In contrast, the local γ-phase area in region B is continuous and distinctly separates the γ´ precipitates on either side. Detailed analysis of concentration profiles in these samples showed some nonequilibrium enrichment of Co in the γ´ phase as well as enrichment of Al in the γ phase. Based on further

analysis, it was concluded that the interconnected γ´ morphology in the water-quenched samples is not due to impingement of separately nucleated equilibrium γ´ precipitates. However, it is also possible to argue that the γ´ precipitates may be forming by classical nucleation and growth with a nonequilibrium partitioning coefficient. Therefore, the origin of the interconnected γ´ morphology remains to be explained. Ordering and subsequent phase separation is one of the mechanisms by which the γ phase can decompose into a mixture of γ phase and L1$_2$ ordered γ´ precipitates.[18] However, further work is necessary to extend this theory to multicomponent nickel-base superalloys.

Computational Analysis of Weldability

Computational models are needed to describe the phenomena that occur during weld cooling (including crystallographic growth, dendrite grain structure, cracking tendency, and solid-state transformations). Dye et al have shown that it is indeed possible to describe weldability of polycrystalline superalloys by describing solidification cracking, carbide liquation, centerline grain boundary formation, porosity formation and inability to obtain full penetration welds using computational modeling.[19,20] These methodologies can be extended to single crystal alloys by coupling with geometrical model and to complex geometries by coupling with detailed heat transfer and mechanics model. These models can then be used to optimize the welding process and process parameters as a function of alloy composition and repair weld geometry. Some of the ongoing research related to this need is presented in this section.

Modeling Weld-Cracking Tendency

Weld cracking results from the competition between the material's resistance to cracking and the mechanical driving force for cracking during weld cooling. The material's resistance is related to the nonequilibrium nature of solidification, the presence of low-melting eutectic films, and the grain structure and high-temperature properties of the alloy. The mechanical driving force is related to local stress-strain development at the trailing edge of the weld pool. Therefore, to model weld cracking, thermomechanical effects along with the metallurgical factors should be considered. Previous research by Feng et al.[9] on local stress-strain conditions, based on macroscopic continuum mechanics, has provided valuable insight into the mechanical driving

force for cracking. In that work, the development of transverse and longitudinal stresses at the weld centerline was calculated as a function of weld cooling. A transverse tensile stress will lead to longitudinal weld centerline cracking. Similarly, a longitudinal tensile stress will lead to transverse weld cracking.

The above analysis was applied to the cracking tendency of N5 laser welds shown in Fig. 5. The temperature variations, σ_{yy} (transverse stress), and σ_{xx} (longitudinal stress) were calculated by using a commercial finite-element software developed for welding (SYSWELD®)[†]. The results for welding speeds of 4.2 mm/s and 12.7 mm/s are shown in Figs. 10 and 11, respectively. As expected, the temperature distribution with a high-speed weld shows an elongated weld pool. The stress plots also show the contour line corresponding to the 99% completion of solidification predicted by assuming the Scheil additivity law and by using the ThermoCalc®[21] software and a commercial nickel thermodynamic database.[22] The results show that when the percentage of solid is ~99%, there is a large area over which the σ_{xx} increases above a tensile stress of 100 MPa [see Fig. 11(c)] in high-speed laser welds but this area is smaller in low-speed laser welds [see Fig. 10(c)]. It is noteworthy that the 100 MPa is almost twice the yield strength of N5 alloy at this temperature. This suggests that if there exists a weak boundary due to the presence of liquid, the probability for transverse cracking will be higher. This is in agreement with the experimentally observed cracking tendency shown in Fig. 5. Although the stress developments are symmetrical about the welding direction, the cracking tendency is not symmetrical. This asymmetry is attributed to an interaction between stresses, crystallographic growth direction and stray grain formation. The results also show that both σ_{xx} and σ_{yy} are always tensile at the trailing edge of the weld pool, even though not of the same magnitude. Therefore, in real welding conditions, the cracking tendency needs to be addressed by a change in metallurgical susceptibility. Recent scanning electron microscopy results [see Fig. 12] have shown that the cracks that occur during laser welding are associated with typical solidification cracking, with some of the surfaces decorated by a liquid film.[14]

[†] http://www.esi-group.com/products/sysweld/index.php

Weld cracking in the mushy liquid-solid mixture zone in the presence of a tensile stress needs to be studied further. For example, it is known that large fractions of liquid do not always lead to weld cracks in the presence of small tensile stress-strain. Instead, the liquid film can heal the cracks by capillary action. However, the presence of a small amount of liquid film may promote the microcracks by rupture and subsequent interconnection of small microcracks. Moreover, the distinction between the effect of stray crystals and the effect of a branched dendritic structure is still unclear. Future work should focus on this most needed estimation of metallurgical cracking susceptibility as a function of composition, weld cooling, and stress state.

Thermodynamic and Kinetic Models

Previous sections addressed the crystallography, grain structure development, phase transformation and thermal stresses that develop during welding. Nevertheless, there is an impetus to relate these phenomena as a function of alloy composition to address following questions. Are all single-crystal nickel-base superalloys prone to weld cracking? Is it possible to design new alloys that have less susceptibility to weld cracking? Will these alloys exhibit similar microstructural characteristics including volume fraction, size and morphology of γ' precipitates? This section describes some of the ongoing research to describe the microstructure evolution during welding with computational thermodynamics and kinetic modeling.

The metallurgical susceptibility for weld cracking can be addressed by using computational thermodynamics and kinetic modeling. In these models, the phase stabilities of different phases are calculated by describing the Gibbs free energy of the phases and by minimizing the overall system free energy using numerical methods. This allows for the calculation of a multicomponent phase diagram. Thermodynamic information is now available for phases that form in single-crystal nickel-base superalloys in an alloy system containing Ni, Al, Co, Cr, Fe, Hf, Mo, Nb, Re, Ta, Ti, W, Zr, B, C, and N.[20] In addition, these calculations can consider the equilibrium between liquid, γ, γ', γ'', β-NiAl, Ni_3Nb, η, Ni_4Mo, δ-NiMo, α(Cr, Mo, W), Laves, σ, μ, R, P, M(C,N), $M_{23}(C,B)_6$, M_6C, $M_7(B,C)_3$, M_2N, M_3B, M_2B (orthorhombic), M_2B (tetragonal), M_3B_2, Cr_5B_3 and TiB_2. An example calculation of a quasi Ni-Al binary diagram for a third-generation single-crystal superalloy N5 (Ni-7.5Co-7Cr-1.5Mo-5W-3.00Re-6.5Ta-0.15Hf)

is shown in Fig. 13. In these calculations, the phase stability between liquid, γ´, β-NiAl, and γ phases were considered. The plot shows that there is only a limited temperature range below the liquidus temperature where the 100% γ phase is present. As a result, there will be increased probability for increase in the solidification temperature range and therefore weld cracking. In addition, thermodynamic calculations can be used to extend theories constitutional undercooling from binary to multicomponent systems, and therefore predict tendency for stray crystal formation.

Recently, Vitek et al. considered the change in equilibrium solidification range due to small variations of alloying elements.[23] An example calculation for another third-generation N6 alloy (Ni-12.5Co-4.2Cr-1.4Mo-6W-5.4Re-7.2Ta-5.75Al-0.15Hf-0.05C-0.004B) is shown in Fig. 14. Interestingly, the plot shows that an increase or decrease in aluminum concentration by 1 wt % leads to a reduction in the solidification temperature range. In contrast, an increase in carbon leads to a decrease in the solidification temperature range. The above calculations can be extended to the nonequilibrium Scheil mode of solidification also. This is illustrated with the following example using the N5 alloy. The equilibrium liquidus temperature for N5 alloy considering all the phases is 1384°C; the solidus temperature is 1335°C. Further calculations, assuming the Scheil law, showed that the solidification range would be lowered to 1100°C due to partitioning of alloying additions to liquid from the γ phase. The calculations also showed the decomposition of liquid to γ + γ´ + P + σ phases toward the final stage of solidification. The presence of P + σ phases compromise the creep-rupture properties. Detailed calculations by changing the alloying element concentrations, one can obtain weld metal composition that does not promote these deleterious phases. It is obvious that this approach can be used for designing filler wires for fusion welding.

After successful fusion welding of a nickel-base superalloy, it is desired to have the weld metal region exhibit creep rupture properties similar to that of the base metal. Therefore, there is a need to understand the decomposition of the γ phase into a mixture of γ + γ´ phases during weld cooling. It is possible to predict the diffusion-controlled growth of the γ´ phase into γ phase by using the DicTra® model.[24] In it, local equilibrium at the interface is assumed and operating tie

lines for the multicomponent equilibrium between γ and γ´ phases are calculated by using the ThermoCalc engine. Furthermore, the diffusion of elements in γ phase, which controls the interface movement, is considered. An example calculation for the growth of γ´ phase in CM247 alloys during a rapid quench is presented here. The geometry of the simulation is shown in Fig. 15(*a*). An interparticle spacing of 20 nm was assumed. This simulation was performed to obtain composition profiles to compare with the APFIM profiles obtained from water-quenched samples. Simulation was performed for an alloy composition of Ni - 9.12 at. % Cr - 9.05% Co - 12.1% Al - 1.0% Ti while cooling from 1090°C to 888°C at a rate of 500°C/s. Further growth of γ´ phase into γ phase below 888°C was ignored due to very low interface velocities in the simulation and numerical instabilities. The calculated volume fraction of γ´ with temperature for this condition is shown in Fig. 15(*b*). The results show rapid growth of γ´ into γ phase below 1090°C (temperature at which the γ´ phase can nucleate). The composition profiles at the end of the simulation at 888°C are shown in Fig. 15(*c*) and are compared with experimentally measured concentration profiles extracted from different sample sections [from Fig. 9(*f*)], as shown in Fig. 15(*d*). The scatter around the fitted experimental concentration profiles in Fig. 15(*d*) is due to statistical scatter in the experimentally measured data. The predicted Cr concentrations range from 12 to 10 at. % in the γ phase. In the case of measured concentrations, they can vary from as high as 30 at. % and as little as 12 at. % in the γ phase. The simulations assumed no diffusion within the γ´ phase; this assumption led to a buildup Cr concentration within the γ´ phase. However, the experimental results exhibit large Cr concentration profiles. In addition, the simulations predict concentration gradients in the γ phase consistent with diffusion-controlled growth (i.e., high Cr concentration near the interface and reduced Cr concentration away from the interface). Interestingly, the measured concentration gradients do not show such a tendency; the Cr concentration near the interface is lower than it is in the bulk of the γ phase. This indicates that the measured concentrations are not typical of those expected from diffusion-controlled growth under local equilibrium conditions at the γ-γ´ interface. Further work is necessary to extend the theoretical models for decomposition of the face-centered-cubic phase into $L1_2$ ordered γ´ precipitates to multicomponent alloys and rapid weld-cooling conditions. This is the focus of the current research.

Summary

An overview was presented of scientific and technical issues related to joining single-crystal nickel-base superalloys. These issues were demonstrated with examples from PWA-1480, CMSX-4, TMS-75, and N5 single-crystal alloys, which are used in the gas turbine industry. A geometric model was used to describe the interaction between crystallography, dendrite grain structure, and weld pool shape. This geometric model, capable of describing dendrite growth directions in any arbitrary welding direction in the crystal reference coordinate system, was used to interpret the grain structure development in an electron beam weld of PWA-1480 and laser welds of N5 alloy. The results show a close correlation between stray grain formations and weld cracking in these alloys. The mechanism for stray grain formation was presented based on solidification theories. The importance of solid-state decomposition of the γ phase on the final $\gamma + \gamma'$ microstructure during rapid cooling conditions was illustrated with detailed microstructural characterization involving atom probe tomography. Computational heat-transfer and stress model calculations show that the presence of tensile stresses and a small amount of liquid along the grain boundaries may lead to weld cracking. Application of computational thermodynamics and a kinetic model was demonstrated to describe solidification characteristics and solid-state decomposition of γ phase to $\gamma + \gamma'$ microstructure under continuous cooling conditions.

Acknowledgments

single-crystal alloy. The authors thank Drs Q. Han and A. S. Sabau for helpful comments on the manuscript.

References

1. D. B. Doll, p. 125 in *Proceedings of Gas Turbine Materials Technology*, ed. P. J. Maziasz, I. G. Wright, W. J. Brindley, J. Stringer, and C. O. Brien, Materials Solutions, Rosemont, Illinois, 1998.

2. S. A. David, J. M. Vitek, S. S. Babu, L. Boatner, and R. W. Reed, *Science and Technology of Welding and Joining* **2** (1997) 79.

3. D. S. Duvall, W. A. Owczarski, and D. F. Paulonis, *Welding Journal*, **53** (1974) 203

4. C. E. Campbell and W. J. Boettinger, *Metallurgical and Materials Transactions A* **31** (2000) 2835

5. S. S. Babu, S. A. David, and M. K. Miller, *Applied Surface Science* **94/95** (1996) 280

6. S. S. Babu, S. A. David, J. M. Vitek, and M. K. Miller, *J. de Physique IV* **6** (1996) C5–253

7. S. A. David, S. S. Babu, and J. M. Vitek, p. 269 in *Proceedings of Mathematical Modeling of Weld Phenomena 4*, ed. H. Cerjak, Materials Modeling Series, IOM Communications Ltd., 1998

8. J. M. Vitek, S. A. David, and L. A. Boatner, *Science and Technology of Welding and Joining*, **2** (1997) 109

9. Z. Feng, S. A. David, T. Zacharia, and C. L. Tsai, *Science and Technology of Welding and Joining* **2** (1997) 109

10. G. M. Goodwin, *Welding Journal* **66** (1987) 33s

11. M. Rappaz, S. A. David, J. M. Vitek, and L. A. Boatner, *Metallurgical Transactions*, **20A** (1989) 1125

12. M. Rappaz, S. A. David, J. M. Vitek, and L. A. Boatner, *Metallurgical Transactions*, **21A** (1990) 1767

13. S. S. Babu and J. M. Vitek, Unpublished research, Oak Ridge National Laboratory, Oak Ridge, TN 37831-6096, USA, 2002

14. J. W. Park, J. M. Vitek, S. A. David, S. S. Babu, Unpublished research, Oak Ridge National Laboratory, Oak Ridge, 2002.

15. J. D. Hunt, *Materials Science and Engineering*, **65** (1984) 75

16. M. Gaumann, R. Trivedi, and W. Kurz, *Materials Science and Engineering*, **A226-228** (1997) 763

17. Kurz, W., and Fisher, D. J., *Fundamentals of Solidification*, Fourth Revised Edition, Trans Tech Publications Ltd, USA, 1998, Page 242

18. S. S. Babu, M. K. Miller, J. M. Vitek, and S. A. David, *Acta Materialia* **49** (2001) 4149

19. O. Hunziker, D. Dye and R. C. Reed, *Acta Materialia* **48** (2000) 4191

20. D. Dye, O. Hunziker, and R. C. Reed, *Acta Materialia* **49** (2001) 683

21. B. Sundman, B. Jansson, and J. O. Andersson, *Calphad* **9** (1985) 153

22. N. Saunders, "Ni-Data Information," Thermotech Ltd., Surrey Technology Center, Guidford, Surrey, GU2 5YG, UK, 1998.

23. J. M. Vitek, S. A. David, and S. S. Babu, "Welding and Weld Repair of Single-Crystal Gas Turbine Alloys," Proceedings of EPRI Welding & Repair Technology Conference, Alabama, 2002

24. J. Agren, *ISIJ International* **32** (1992), 291.

Figures
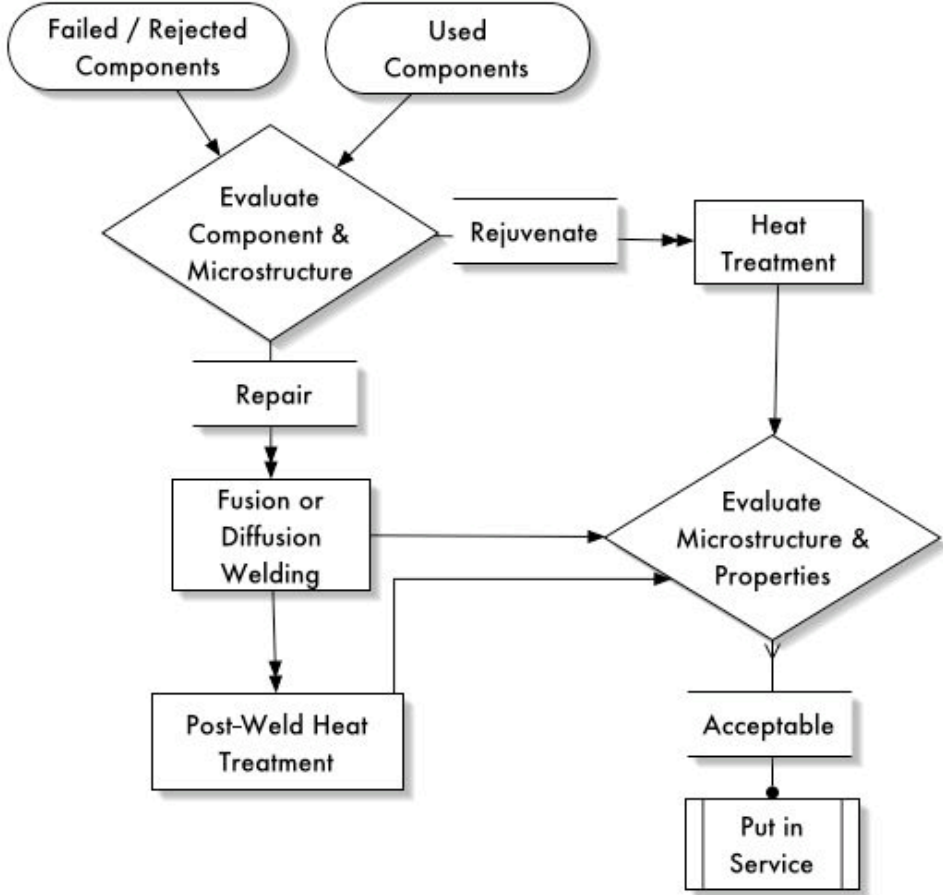
Fig. 1   Flow chart for reuse and reclamation of used, failed, and rejected nickel-base superalloy components for land-based turbines
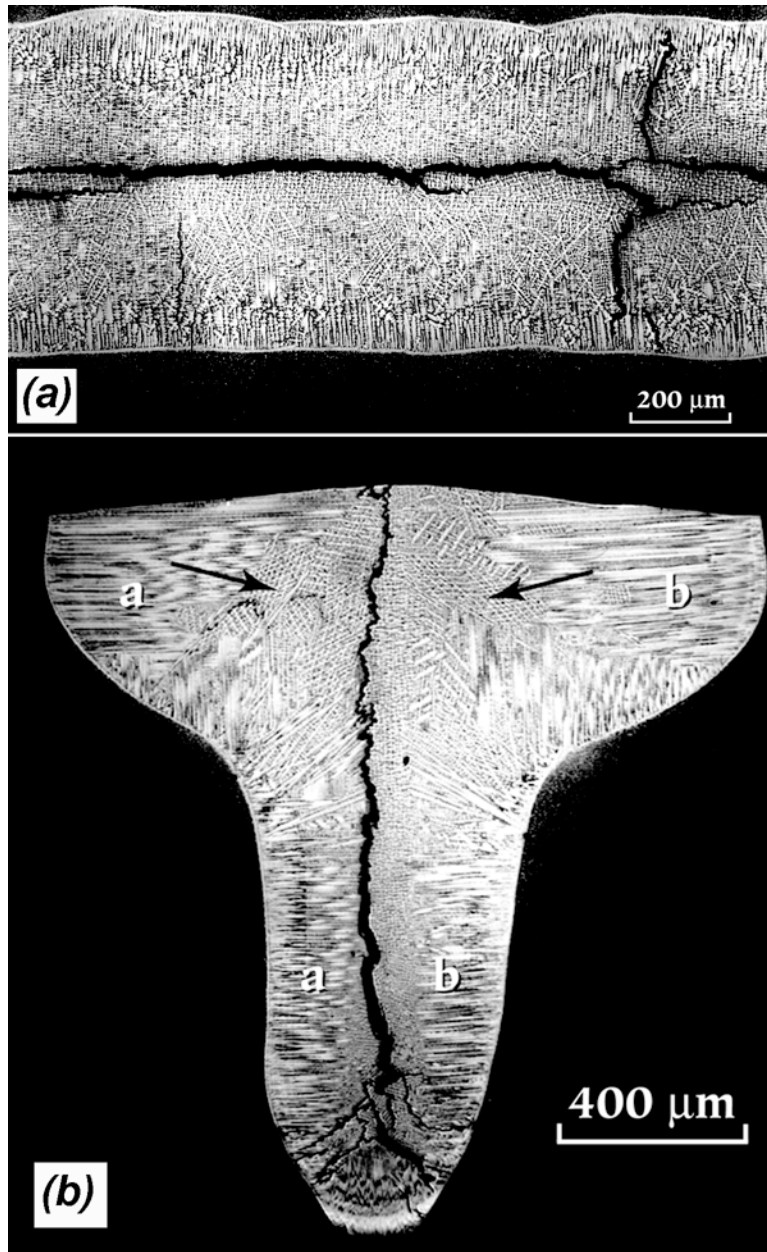
Fig. 2   Optical micrographs of (*a*) top surface and (*b*) transverse cross section of PWA-1480 electron beam welds made without preheat, showing the extensive centerline cracking in the weld metal region. In (*b*), the regions "a" and "b" exhibit epitaxial growth, and the arrows point to the stray crystal regions where the cracking was observed.
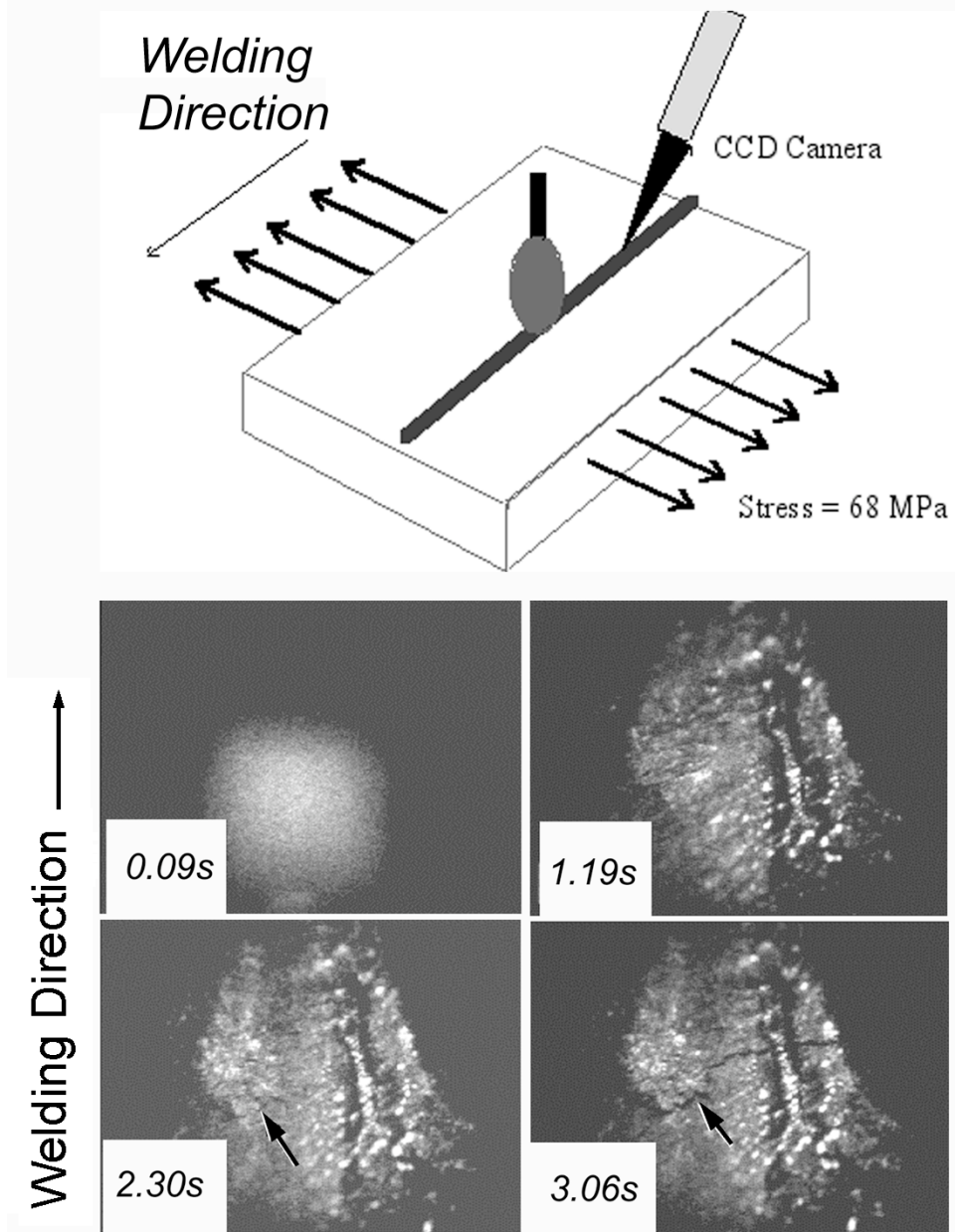
Fig. 3   Schematic illustration and results of in situ crack monitoring during welding of an
experimental nickel-base superalloy. The charge-coupled device camera was focused
on the weld-metal region near the start region of the weld. The surface images of the
welds were recorded by a video camera. The snapshots at four different times are
shown. The arrows in the images show the location of the crack.

(a)

200 μm

(b)

(c)
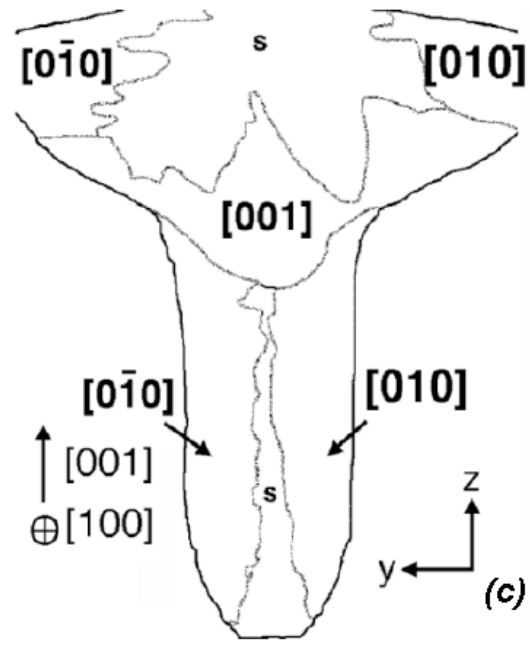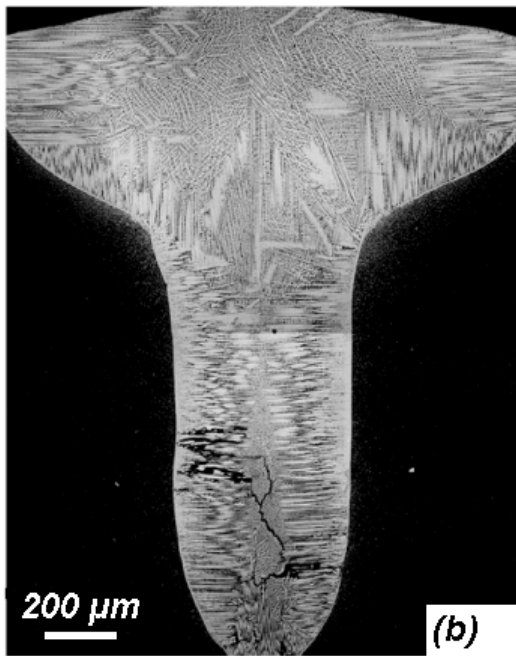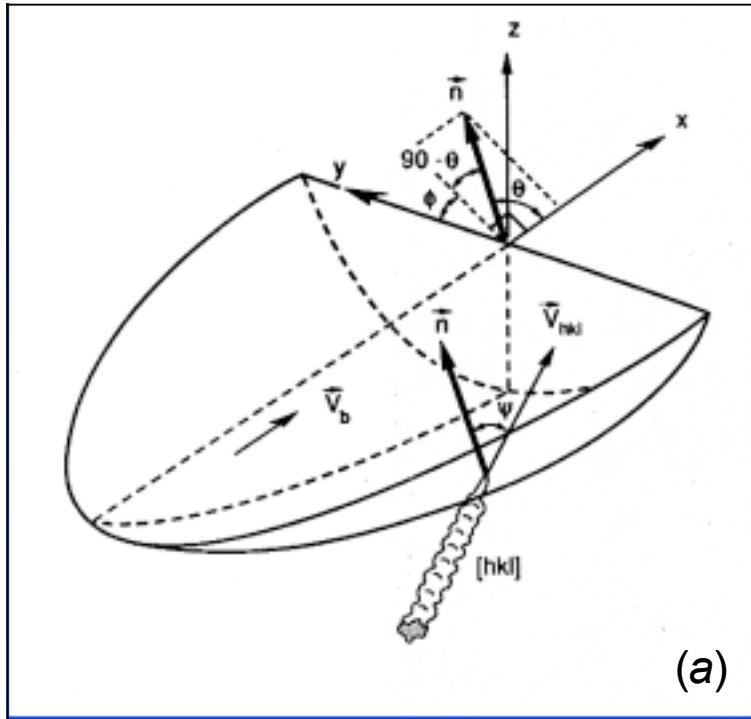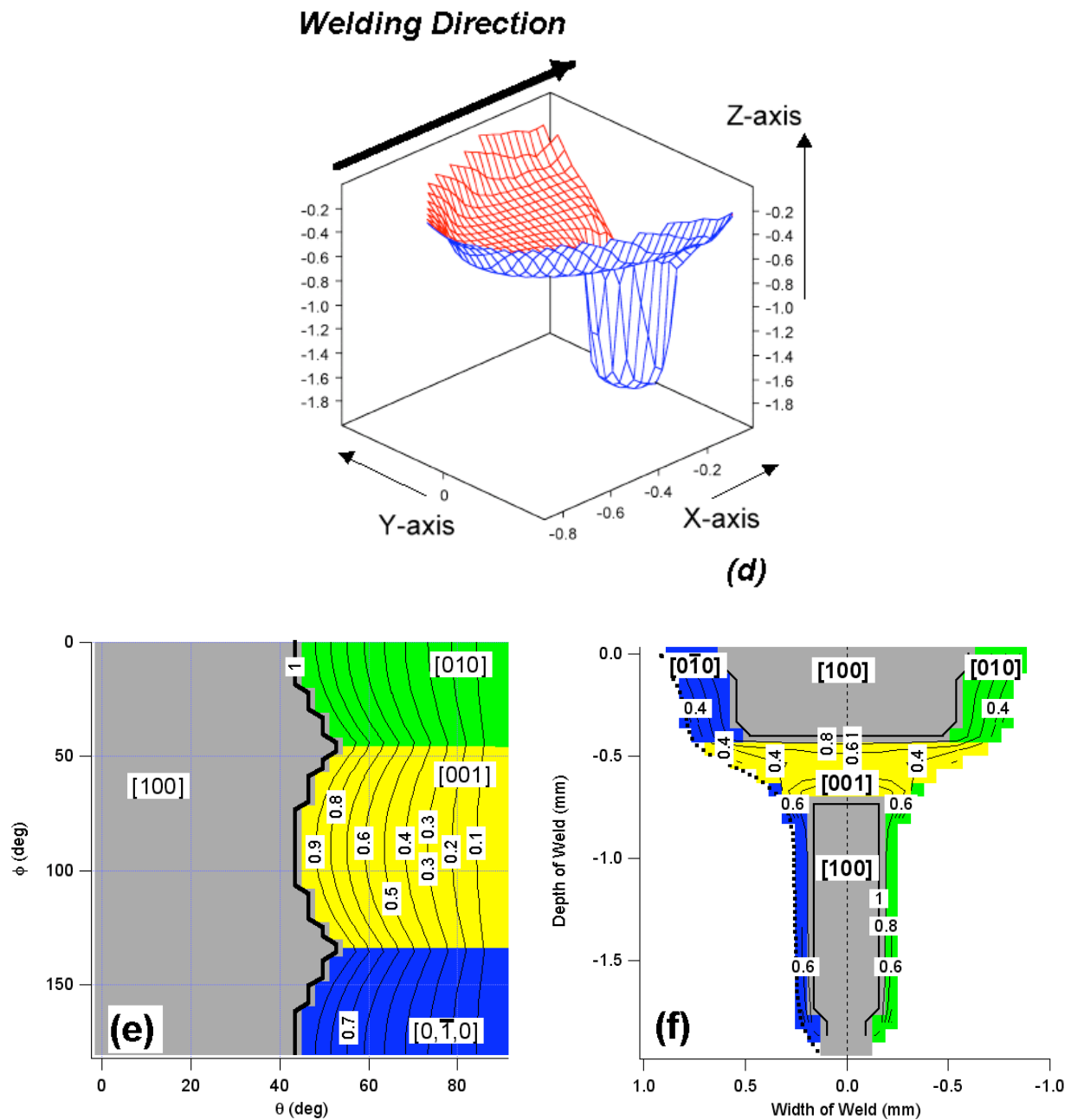
Fig. 4   (*a*) Schematic illustration of geometric model for prediction of dendrite growth direction. (*b*) Optical micrograph of the dendritic microstructure from a PWA-1480 electron beam weld. (*c*) Interpretation of the dendrite growth patterns based on observed dendrite morphology. (*d*) Three-dimensional representation of weld pool profile, (*e*) Dendrite growth map for <001> directions based on the geometry model as a function of θ and ψ. (*f*) Predicted dendrite growth directions at different locations as a function of *y* and *z* axes

21
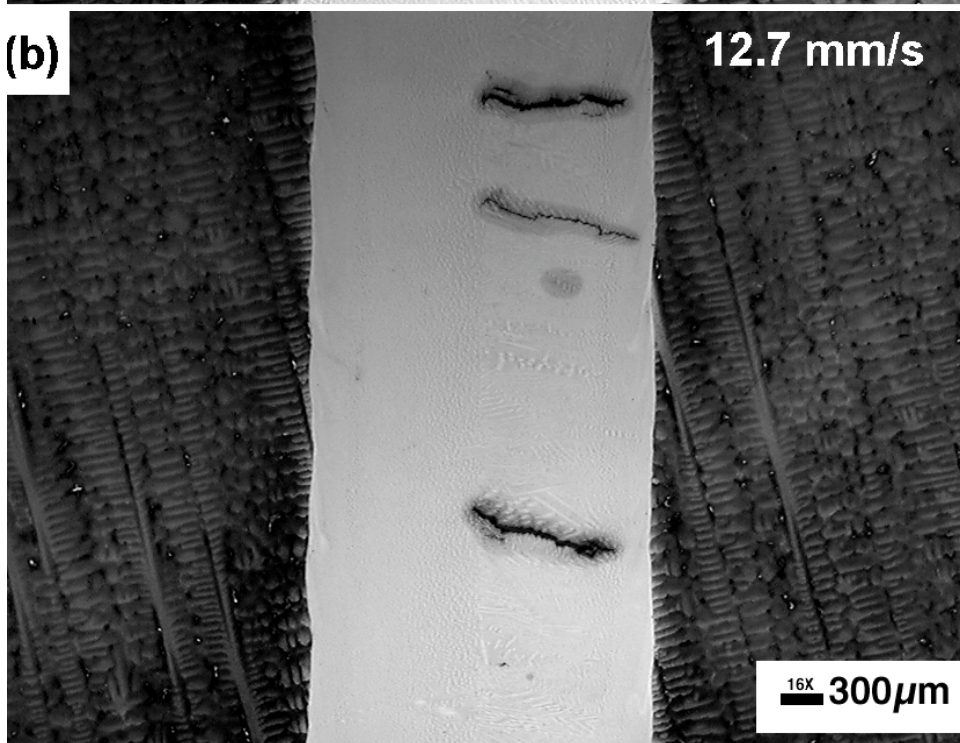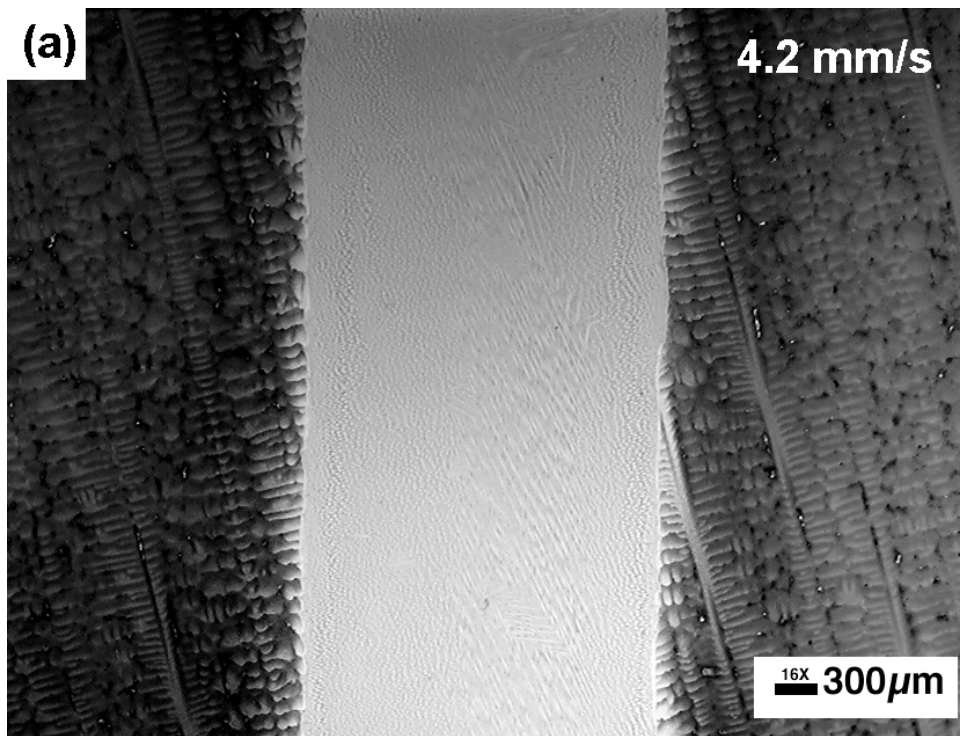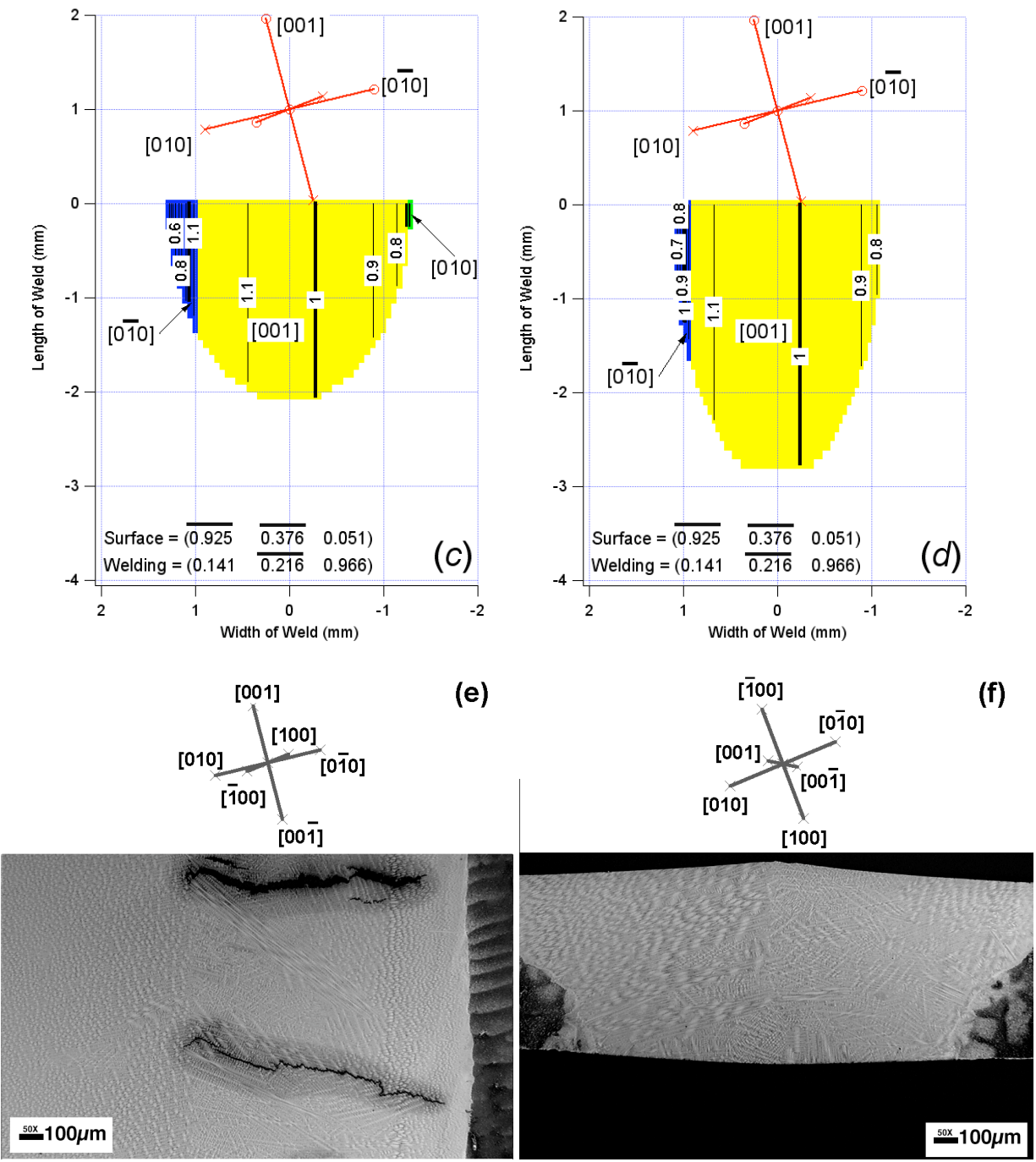
Fig. 5   Optical micrograph of autogeneous laser welds made on N5 alloy with welding speeds of (*a*) 4.2 mm/s and (*b*) 12.7 mm/s. Results from dendrite growth model for weld geometry(surface view) with (*c*) 4.2 mm/s and (*d*) 12.7 mm/s. Micrographs and approximate <001> growth directions for the welds made at 12.7 mm/s (*e*) surface and (*f*) cross sectional views.
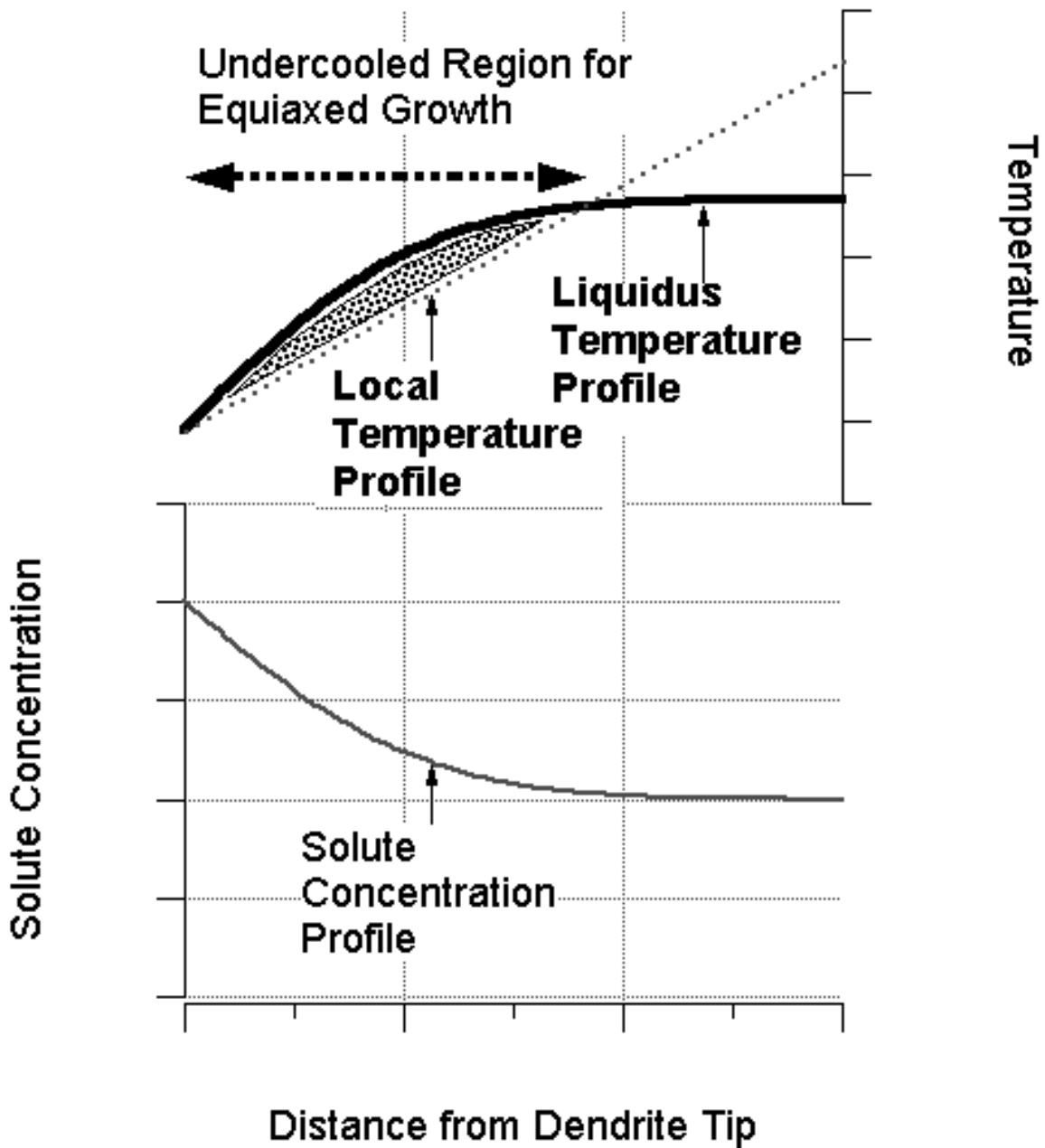
Fig. 6   Schematic illustration of conditions for the promotion of equiaxed dendritic growth based on constitutional undercooling: (bottom) solute concentration profile ahead of the dendrite in the liquid (top) Corresponding depression of liquidus temperature and the local temperature profile given by the temperature gradient across the solid-liquid boundary. The region over which the local temperature is lower than the liquidus temperature profile is ideal for the equiaxed dendrite nucleation (i.e., stray grain formation).
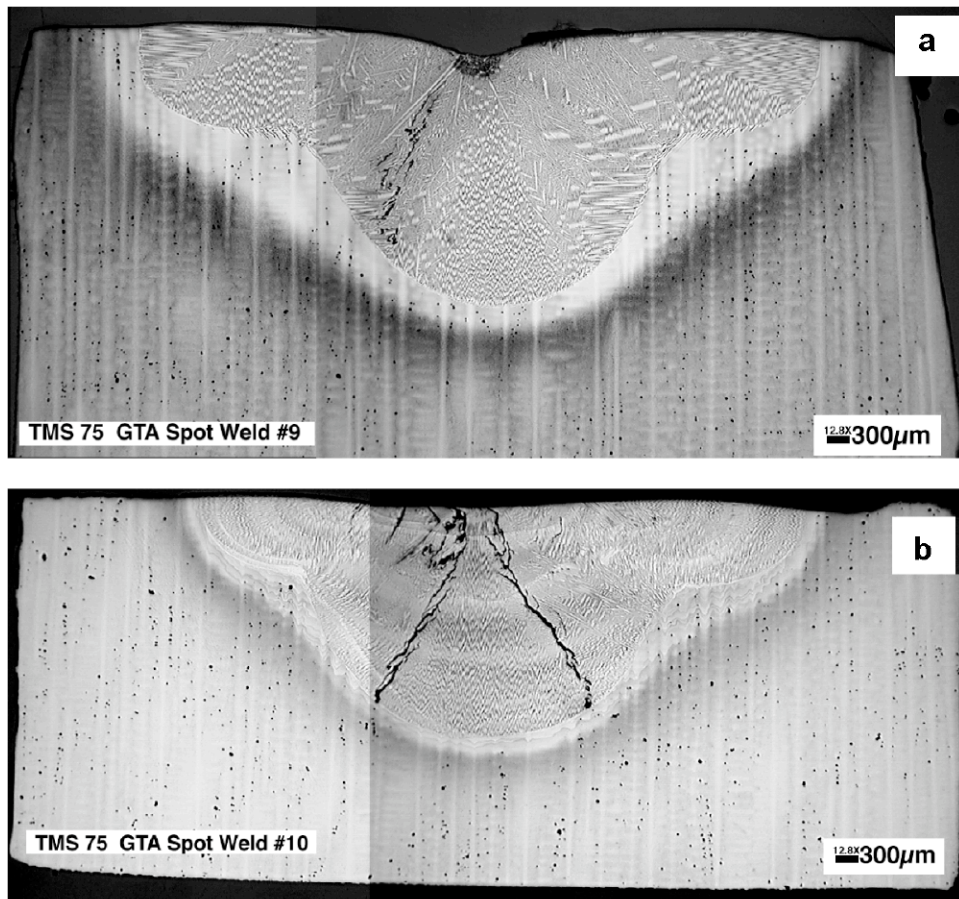
Fig. 7   Optical micrograph of spot welds made on TMS-75 single-crystal nickel-base superalloy bars under (*a*) a rapid cooling condition induced by sudden arc extinction and (*b*) a slow cooling condition induced by a gradual slope down of welding current.
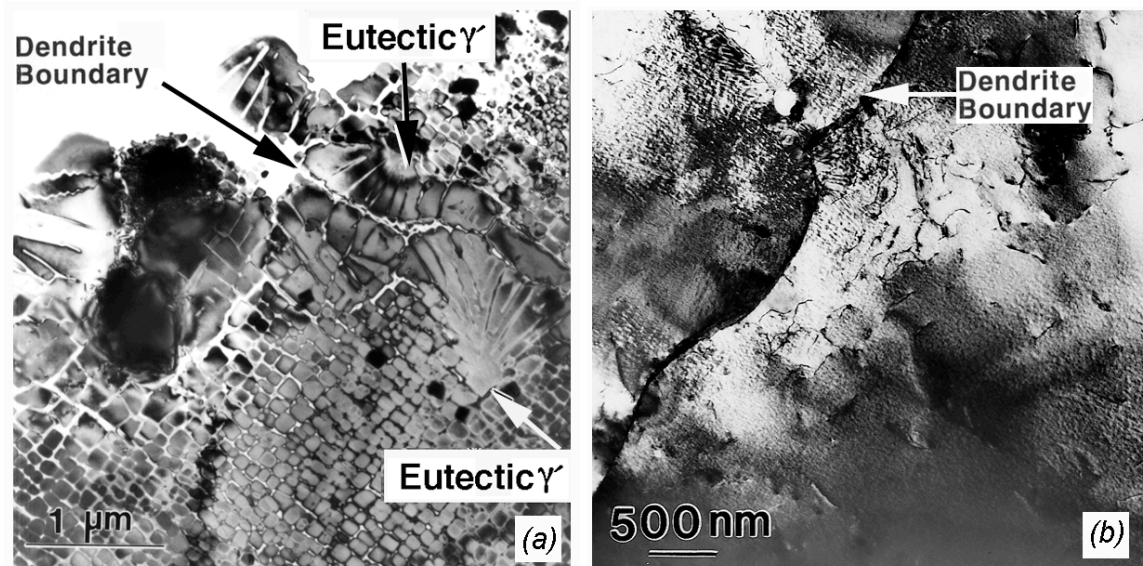
Fig. 8 Transmission electron micrographs of (*a*) a PWA-1480 electron-beam weld showing the well-developed cuboidal γ´ microstructure and eutectic γ+γ´ microstructure along the dendrite boundary and (*b*) a CMSX-4 pulsed-laser weld showing the negligible amount of eutectic γ+γ´ microstructure along the dendrite boundaries and very fine γ´ precipitates within γ matrix.
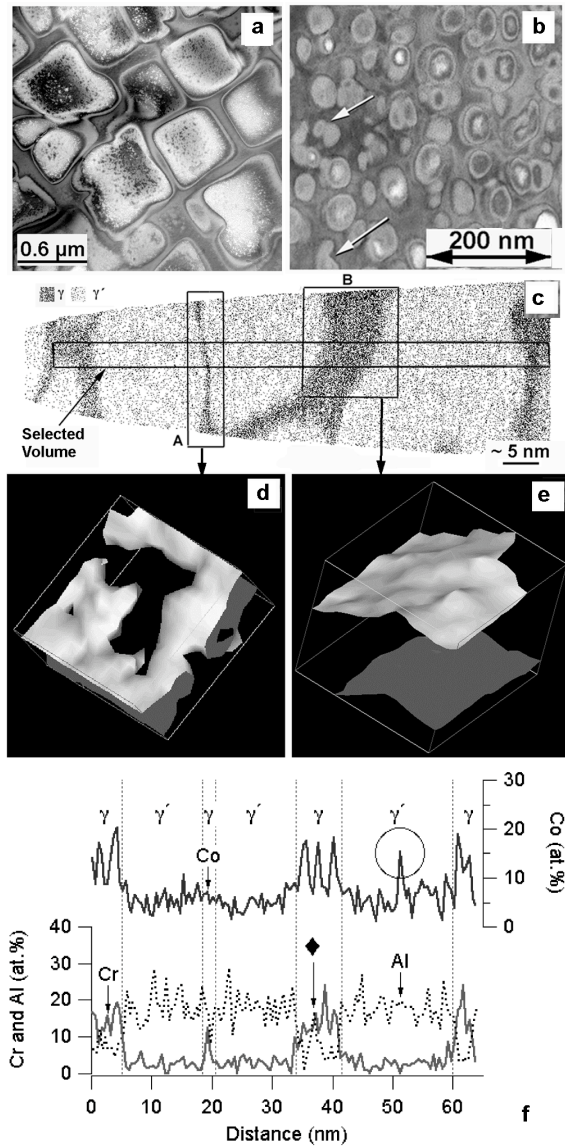
Fig. 9   Analyses of CM247 alloys in different conditions: Transmission electron micrographs
         along the [001] zone axis (*a*) base metal after standard heat treatment and (*b*) after
         solutionizing at 1300°C and water-quenched. Note the complex γ´ precipitate
         morphology marked by arrows in the water-quenched condition. (*c*) Atom-probe
         tomography map from a water-quenched CM247DS sample showing Cr atoms. The
         atom image shows the presence of γ´ precipitates (Cr-depleted light) in a γ (Cr-enriched
         dark) matrix. The iso-concentration surfaces corresponding to 15 at. % Cr are shown
         from (*d*) region A and (*e*) region B. (*f*) The concentration profiles of Cr, Al and Co
         through the selected volume shown in (*c*).

27
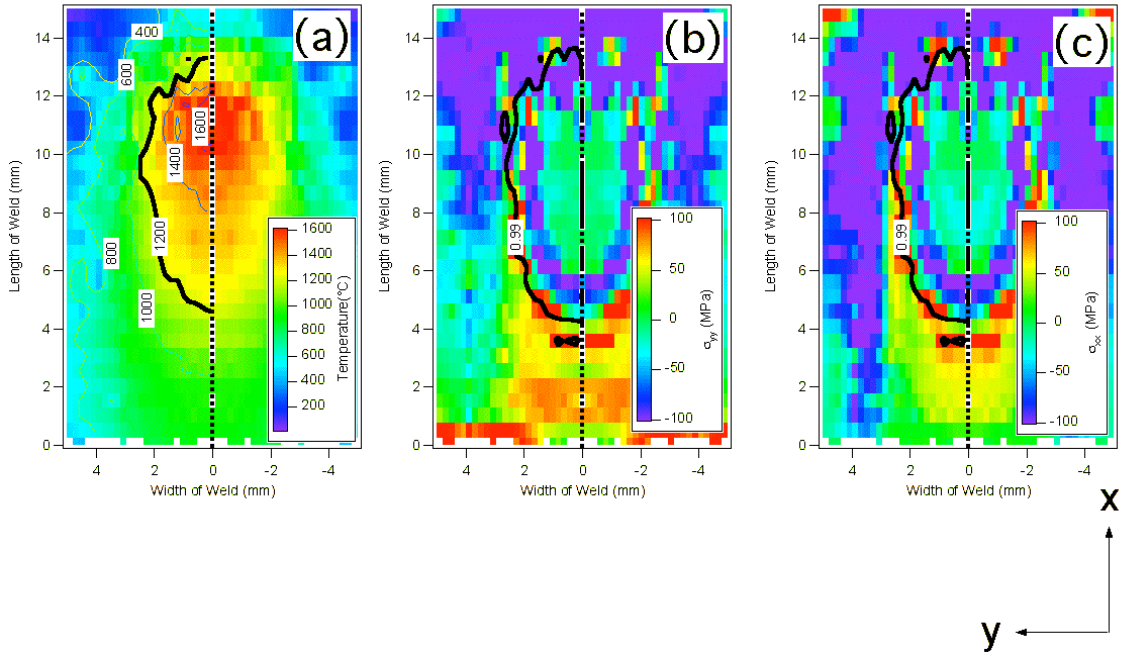
Fig. 10 Results from a computational heat transfer and stress model for an autogenous laser weld made on N5 alloy at a speed of 4.2 mm/s. (*a*) Temperature distribution and corresponding (*b*) σ_{yy} and (*c*) σ_{xx} at different locations.
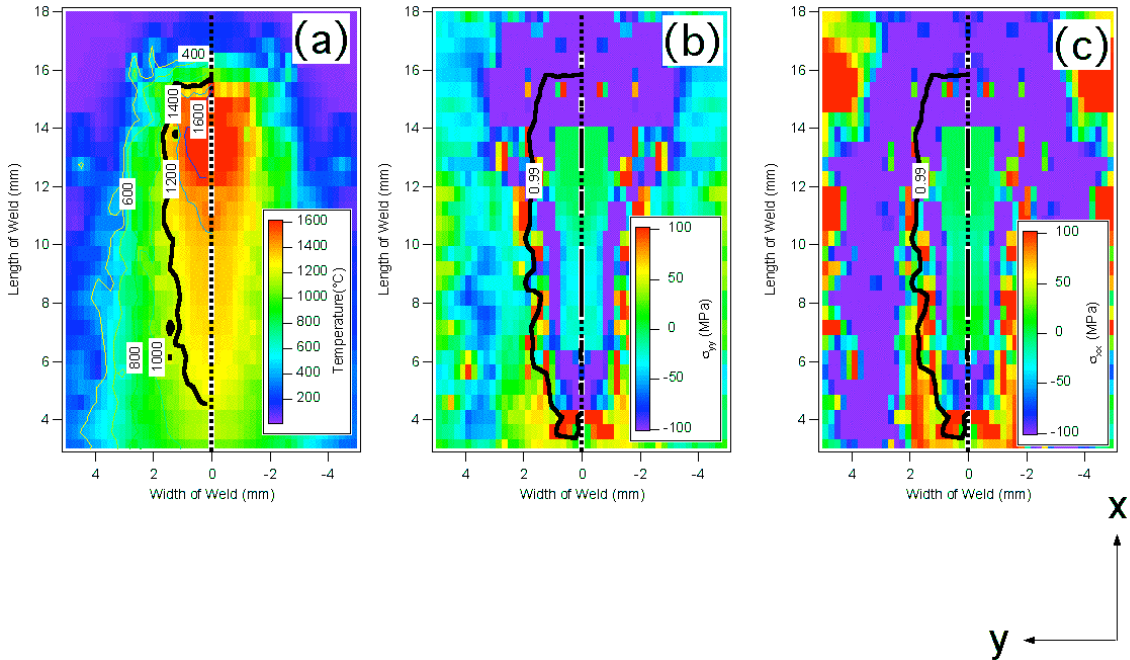
Fig. 11 Results from a computational heat transfer and stress model for an autogenous laser weld made on N5 alloy at a speed of 12.7 mm/s. (*a*) Temperature distribution and corresponding (*b*) σ_{yy} and (*c*) σ_{xx} at different locations.
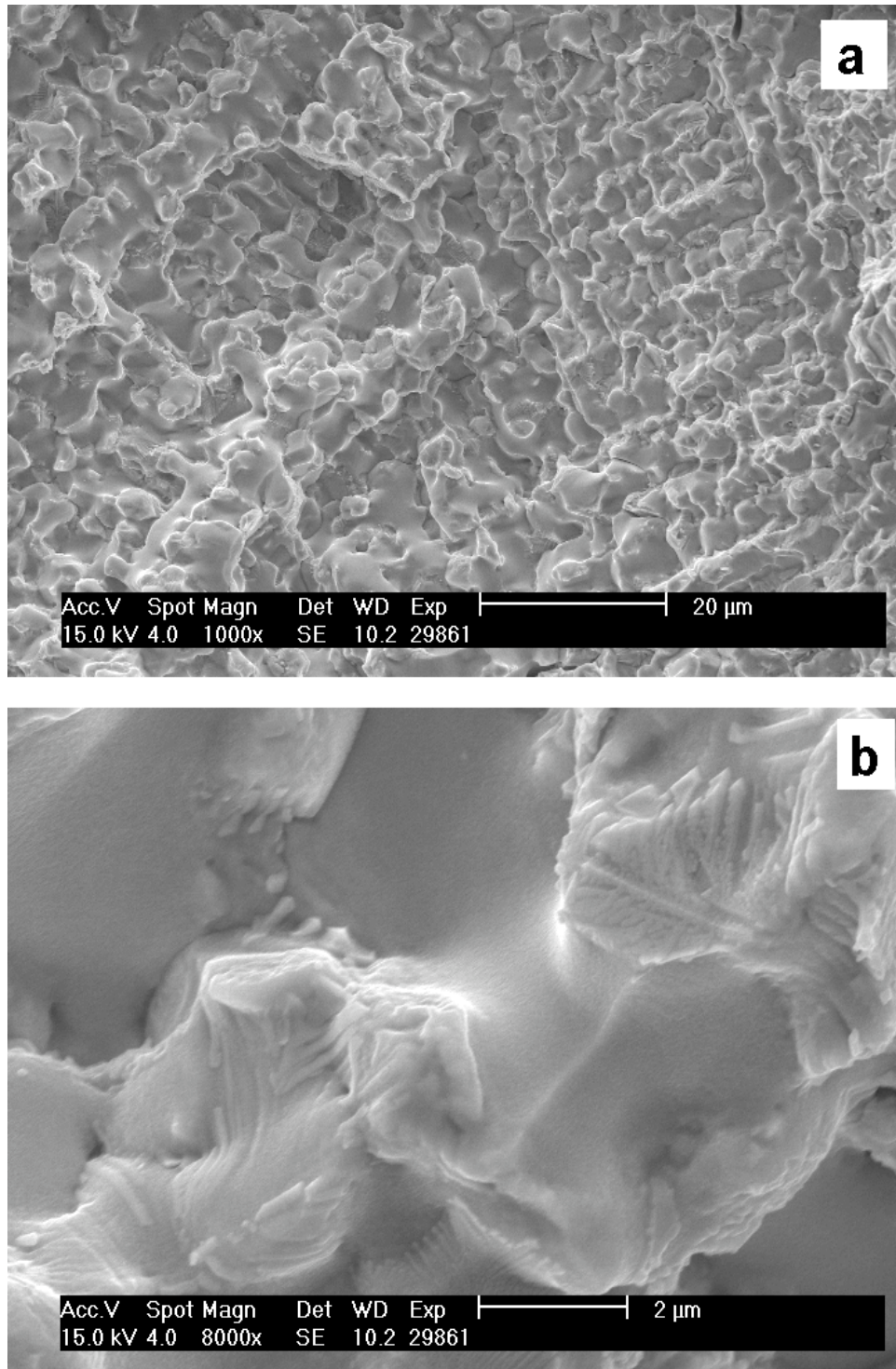
Fig. 12   Scanning electron micrograph from the cracked surface of a N5 laser weld at (*a*) low magnification showing dendritic morphology and (*b*) high magnification showing smooth dendrite surface and some features resembling eutectic structure.
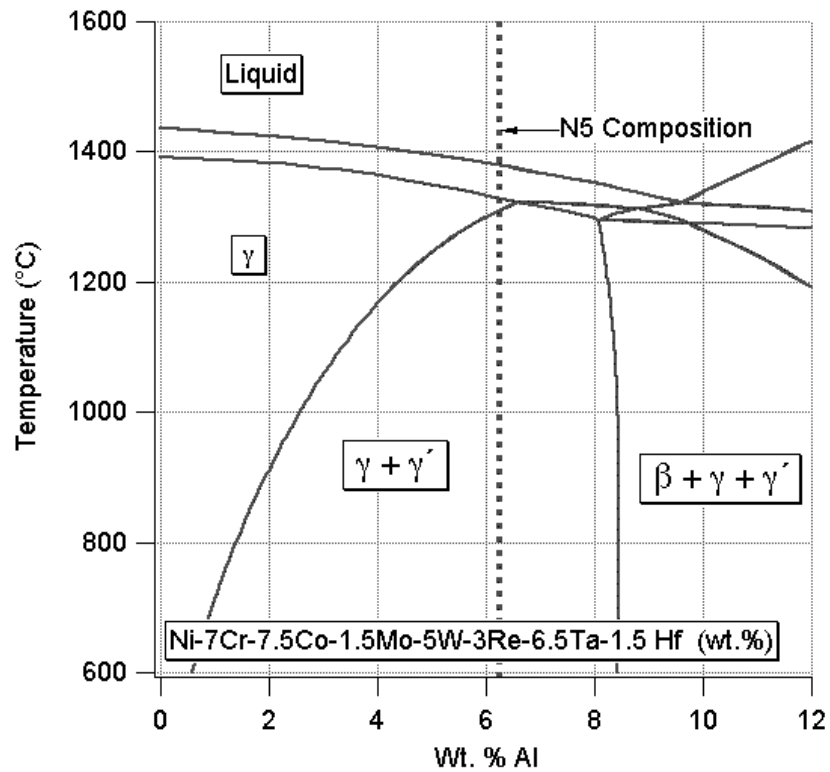
Fig. 13   A quasi-binary diagram for Ni-X$_i$-Al for N5 alloy that shows stability of liquid, γ, γ′, and β (NiAl) phase as a function of temperature and aluminum concentration.
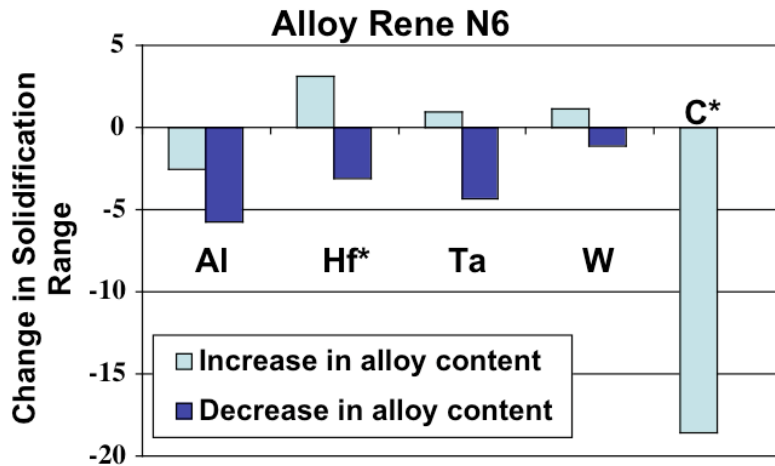
Fig. 14   Change in solidification temperature range for small changes in concentration of various elements from nominal composition of N6 alloy
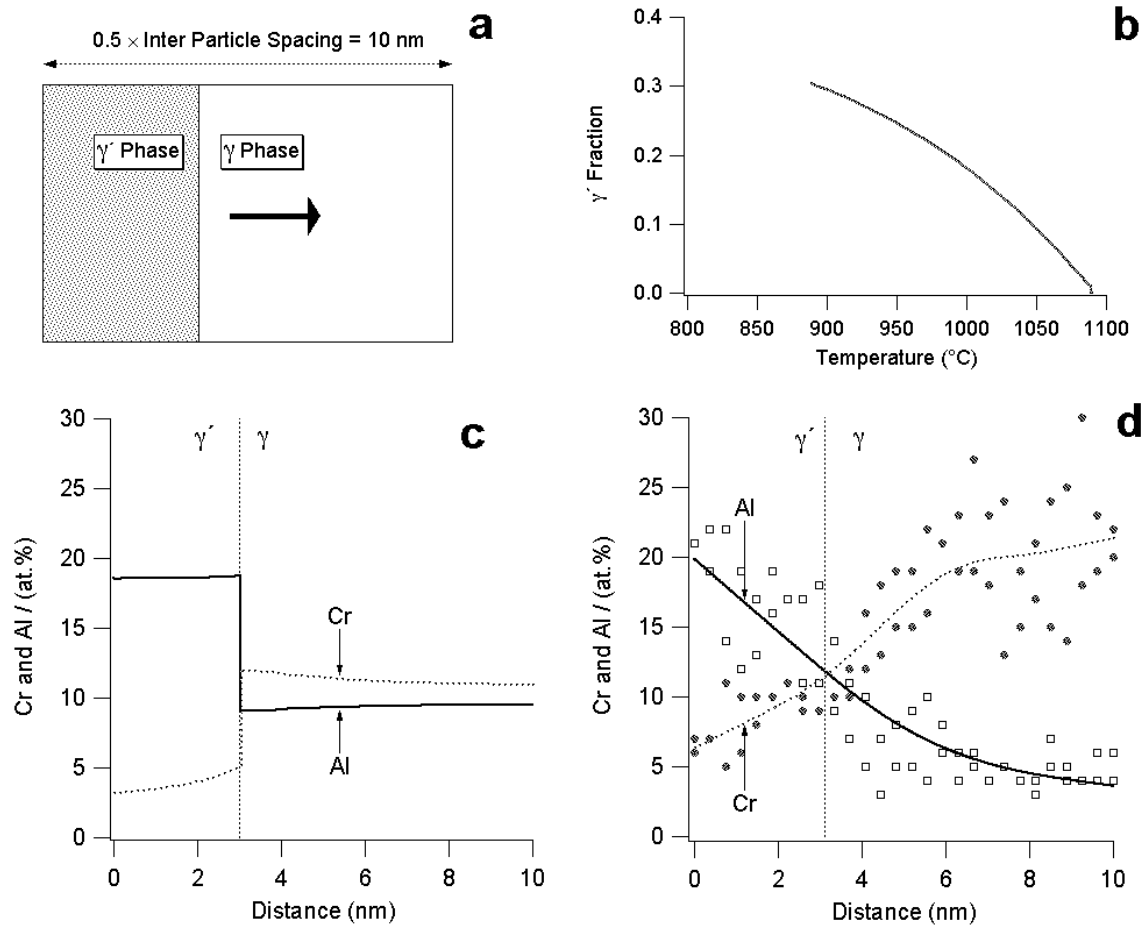
Fig. 15 (*a*) Schematic illustration of the geometry used for simulating diffusion-controlled growth of γ′ phase into γ phase. (*b*) Predicted variation of γ′ volume fraction with time as the CM247 alloy cools from 1090°C (γ′ solvus temperature) at a linear rate of 500°C/s. (*c*) Predicted concentration profiles of Cr and Al at 888°C after cooling from 1090°C at a rate of 500 °C/s. (*d*) Extracted concentration profiles of Cr and Al from atom probe tomography data over many sections from water-quenched sample shown in Fig. 9(*f*).

Figure Captions